magnetism

MDPI

Article

Magnetism of Tetragonal β-Fe_3Se_4 Nanoplates Controllably Synthesized by Thermal Decomposition of (β-Fe_2Se_3)$_4$[Fe(tepa)] Hybrid

Qifeng Kuang [1], Xiaoling Men [1], Xiaolei Shang [1], Bing Yang [1], Yangtao Zhou [1], Bo Zhang [2], Zhiwei Li [2], Da Li [1,*] and Zhidong Zhang [1,*]

[1] Shenyang National Laboratory for Materials Science, Institute of Metal Research, Chinese Academy of Sciences, and School of Materials Science and Engineering, University of Science and Technology of China, 72 Wenhua Road, Shenyang 110016, China; qfkuang18b@imr.ac.cn (Q.K.); xlmen19b@imr.ac.cn (X.M.); xlshang20s@imr.ac.cn (X.S.); byang@imr.ac.cn (B.Y.); ytzhou@imr.ac.cn (Y.Z.)

[2] Key Lab for Magnetism and Magnetic Materials of the Ministry of Education, Key Lab for Special Functional Materials and Structure Design of the Ministry of Education, School of Physical Science and Technology, Lanzhou University, Lanzhou 730000, China; zhangb2016@lzu.edu.cn (B.Z.); zweili@lzu.edu.cn (Z.L.)

* Correspondence: dali@imr.ac.cn (D.L.); zdzhang@imr.ac.cn (Z.Z.)

Abstract: We report magnetism of tetragonal β-Fe_3Se_4 nanoplates controllably synthesized by thermal decomposition at 603 K of inorganic–organic (β-Fe_2Se_3)$_4$[Fe(tepa)] hybrid nanoplates (tepa = tetraethylenepentamine). (β-Fe_2Se_3)$_4$[Fe(tepa)] hybrid precursor and β-Fe_3Se_4 nanoplates are in single crystal features as characterized by selected area electron diffraction. Rietveld refinements reveal that ordered inorganic–organic (β-Fe_2Se_3)$_4$[Fe(tepa)] hybrid nanoplates are in a tetragonal layered crystal structure with a space group of I4cm (108) and room-temperature lattice parameters are a = 8.642(0) Å and c = 19.40(3) Å, while the as-synthetic tetragonal β-Fe_3Se_4 nanoplates have a layered crystal structure with the P4/nmm space group, and room-temperature lattice parameters are a = 3.775(8) Å and c = 5.514(5) Å. Magnetic measurements show the weak ferrimagnetism for (β-Fe_2Se_3)$_4$[Fe(tepa)] hybrid nanoplates at room temperature, while the as-synthetic β-Fe_3Se_4 nanoplates are antiferromagnetic in a temperature range between 120 and 420 K but in a ferrimagnetic feature below ~120 K. The as-synthetic β-Fe_3Se_4 nanoplates are thermally instable, which are transformed to ferrimagnetic β-Fe_3Se_4 nanoplates by annealing at 623 K (a little higher than the synthetic temperature). There is an irreversible change from antiferromagnetism of the as-synthetic β-Fe_3Se_4 phase to the ferrimagnetism of the as-annealed β-Fe_3Se_4 phase in a temperature between 420 and 470 K. Above 470 K, the tetragonal β-Fe_3Se_4 phase transforms to monoclinic Fe_3Se_4 phase with a Curie temperature (T_C) of ~330 K. This discovery highlights that crystal structure and magnetism of Fe-Se binary compounds are highly dependent on both their phase compositions and synthesis procedures.

Keywords: magnetism; iron selenides; crystal structure; nanoplates

Citation: Kuang, Q.; Men, X.; Shang, X.; Yang, B.; Zhou, Y.; Zhang, B.; Li, Z.; Li, D.; Zhang, Z. Magnetism of Tetragonal β-Fe_3Se_4 Nanoplates Controllably Synthesized by Thermal Decomposition of (β-Fe_2Se_3)$_4$[Fe(tepa)] Hybrid. *Magnetism* **2022**, *2*, 31–44. https://doi.org/10.3390/magnetism2010003

Academic Editor: Gerardo F. Goya

Received: 27 November 2021
Accepted: 25 January 2022
Published: 1 February 2022

1. Introduction

The synthesis and characterization of iron selenides are interesting topics in materials sciences, due to their outstanding electrical and magnetic properties, which are sensitively dependent on their phase compositions and crystal structures [1–4]. It is known that hexagonal Fe_7Se_8 is in the ferrimagnetism with the Curie temperature (T_C) at ~460 K and a spin-reorientation occurs around 130 K for Fe_7Se_8 [5], while monoclinic Fe_3Se_4 has a T_C at ~320–340 K [4,6]. Due to large uniaxial magnetocrystalline anisotropy constant (1×10^7 erg/cm^3 at 10 K), Fe_3Se_4 nanostructures [7,8] and Cr-doped Fe_3Se_4 compounds [9,10] have received attention owing to the realization of a large coercivity as potential rare-Earth-free permanent magnets. The ferrimagnetism of Fe_3Se_4 and Fe_7Se_8

originates from the ferromagnetically aligned spins within the c-plane and antiferromagnetically coupled adjacent Fe planes with ordered iron vacancies [11]. Tetragonal β-FeSe with a PbO structure is intriguing for the simplest layered crystal structure with the P4/nmm space group in the iron-based superconductors [2]. The superconductivity of β-FeSe is sensitively dependent on the crystal structure [12] and stoichiometry [13]. Theoretical studies show that tetragonal β-FeSe is nonmagnetic, but ferromagnetism is present in the hexagonal NiAs-type α-FeSe with the T_C of 420 K [14]. Se-rich FeSe films exhibit a ferrimagnetic order with the T_C ~325 K [15], but ordered Fe vacancies lead to composition-dependent antiferromagnetic orders for some tetragonal β-$Fe_{1-x}Se$ ($0 < x < 0.2$) superstructures, such as β-Fe_4Se_5, at low temperatures [13,16]. However, the effect of the composition x on the magnetism of β-$Fe_{1-x}Se$ was not studied enough due to difficult synthesis for single phase β-$Fe_{1-x}Se$. β-Fe_3Se_4 superstructures serve as components in the intercalated compound $TlFe_{1.5}Se_2$, which show two possible states, in which the square superstructure of $\sqrt{2} \times \sqrt{2}$ has lower energy than the rhombus ordered pattern ($\sqrt{2} \times 2\sqrt{2}$) [17]. Antiferromagnetic order of $AFe_{1.5}Se_2$ (A = Tl, K, Rb, or Cs) is driven by the Se-bridged antiferromagnetic superexchange interactions between Fe moments [17]. The selected area electron diffraction (SAED) pattern of square β-Fe_3Se_4 superstructure along the c-axis is similar to that of superconducting tetragonal β-FeSe, except that the absented (h00) and (0k0) with h odd and k odd are now visible due to Fe vacancy order [16]. A previous work reveals that $FeSe_2$ chains were used to coordinate with Fe-amine (amine = ethylenediamine (en), diethylenetriamine (dien) or tris(2-aminoethyl)amine (tren)) complexes for hybrid $(FeSe_2)_2[Fe(en)_2]$ [18], $(FeSe_2)_2[Fe(dien)_2]$ and $(FeSe_2)_2[Fe(tren)]$ [19]. More recently, we reported that tetragonal β-Fe_3Se_4 superstructures can be used as inorganic building units to construct the room temperature ferrimagnetic $(β\text{-}Fe_3Se_4)_4[Fe(teta)_{1.5}]$ (teta = triethylenetetramine) [20]. Moreover, the $FeSe_x$ inorganic building units can be changed from $FeSe_2$ chains to β-Fe_2Se_3 and β-Fe_3Se_4 by tuning the stoichiometric ratio of Fe and Se precursors in the organic diethylenetriamine (dien) system [21]. However, the monoclinic phase of Fe_3Se_4 but not tetragonal phase was obtained by direct thermal decomposition of the $(β\text{-}Fe_3Se_4)_4[Fe(teta)_{1.5}]$ and the $Fe_3Se_4(dien)_2$ hybrid materials at a temperature higher than their decomposition temperatures [20,21]. There was previously a rare report on the magnetic information of tetragonal β-Fe_3Se_4 single phase [16].

Here, we design and synthesize a new ordered inorganic–organic $(β\text{-}Fe_2Se_3)_4[Fe(tepa)]$ hybrid material. Tetragonal β-Fe_3Se_4 nanoplates were synthesized by thermal decomposition of the hybrid precursor in a tepa solution at 603 K. Tetragonal β-Fe_3Se_4 nanoplates show interesting magnetism due to tetragonal crystal structure and disordered distribution of iron vacancies, which is much different from that of monoclinic Fe_3Se_4. Our study provides guidance for future applications in such a chemical solution for controllable synthesis of tetragonal β-$Fe_{1-x}Se$ functional materials in a wide composition range with varied crystal structure but the same composition.

2. Materials and Methods

Commercially available reagents including iron acetylacetonate ($Fe(acac)_3$, 98%) and SeO_2 (powder, 99.9%) were purchased from Aladdin Reagent company (Shanghai, China). Tetraethylenepentamine ($C_8H_{23}N_5$, tepa), ethanol (99.7%) and acetone (99.8%) were purchased from Sinopharm Chemical Reagent Co. Ltd. (Shenyang, China). All chemicals were used as received without any further purification.

In a typical reaction for a new ordered inorganic–organic $(β\text{-}Fe_2Se_3)_4[Fe(tepa)]$ hybrid material, 2162.7 mg of $Fe(acac)_3$ and 888.3 mg of SeO_2 with the Fe/Se molar ratio of 6:8 were mixed in 80 mL of tepa in a 250 mL four-neck flask. Under a nitrogen flow, the mixture solution was heated to 393 K and kept for 1 h to remove moisture and oxygen. Then, the temperature was slowly raised to 573 K in a period time of 50 h and maintained for 3 h to obtain product with good crystallization. The solution was cooled to room temperature by removing the heating source. The precipitates were separated from reaction solution by centrifugation at 8000 rpm. A ThermoFisher inductively coupled plasma (ICP)

spectroscopy gave a concentration of 0.0208 and 0.0715 mg mL^{-1}, respectively for Fe and Se ions left in the yellow transparent supernatant above the precipitates, suggesting that all the Fe and Se atoms in the starting materials have combined in the hybrid product. The precipitates were rewashed by 15 mL of acetone for four times.

For the synthesis of tetragonal Fe_3Se_4 nanoplates, the hybrid precursor was dispersed in 80 mL of tepa in a 250 mL four-neck flask. Under a nitrogen flow, the mixture solution was heated to 573 K at a ramping rate of 10 K min^{-1} and kept for 3 h. Then, the temperature was raised to 603 K in a period time of 12 h and maintained for 3 h. Finally, the product was cooled to room temperature by removing the heating source. The resultant product was precipitated by centrifugation at 8000 rpm and washed with 15 mL of acetone for five times. Both the hybrid precursor and the thermal decomposed product were dried in vacuum at room temperature and store in a glovebox with an argon atmosphere for further characterization.

Powder X-ray diffraction (XRD) was performed on a D/Max-2400 diffractometer (Rigaku Inc., Tokyo, Japan) equipped with a Cu K_α radiation source at room temperature. The program Rietica was used to refine the crystal structure of the products. The size and morphology of the products were examined by a JSM 6301F field-emission scanning electron microscope (FESEM) (JEOL Inc., Tokyo, Japan) system and a Tecnai G2 F20 transmission electron microscope (TEM) (FEI Inc., Hillsboro, OR, USA) at 200 kV. The Fourier transform infrared (FTIR) spectrum was recorded on a Nicolet iN10 MX & iS10 spectrometer using the KBr pellet technique (Thermo Fisher Inc., Waltham, MA, USA). Elemental compositions of the products were analyzed by an Oxford energy dispersive X-ray (EDX) spectroscopy. Thermal gravimetric analysis (TGA) was carried out on a STA6000 thermal analyzer (PerkinElmer Inc., Waltham, MA, USA) with heating rate of 10 K min^{-1} between 300 and 800 K. Temperature-dependent magnetization in the field-cooling (FC) and zero-field-cooling (ZFC) modes (H = 0.1 and 50 kOe) and static magnetic measurements of the products were performed using a vibrating sample magnetometer (VSM) standard option in a physical property measurement system (PPMS) (Quantum Design Inc., San Diego, CA, USA) equipped with a superconducting magnet with a maximum magnetic field of 140 kOe in a temperature range between 5 and 400 K. The magnetization versus temperature curves of the Fe_3Se_4 nanoplates in a temperature range between 300 and 720 K were collected using the VSM with the oven option in a high vacuum state during the oven operation.

3. Results

3.1. Structure Properties

SEM (Figure 1a) and TEM images (Figure 1b) illustrate that the hybrid precursor possesses a square plate shape with a size of about 70–100 nm for thickness and 1–6 μm for length. Fourier transform infrared (FTIR) spectrum (Figure 2) presents characteristic peaks of tepa featured by the vibration bands of -CH_2-, -NH_2, and -NH. The bands at 2915, 2860 and 1453 cm^{-1} are ascribed to the stretching vibration and C–H deformation of $-CH_2$ in the tepa chain. Two bands at 3436 and 3273 cm^{-1} are caused by asymmetric and symmetric bending vibrations of $-NH_2$, while the band at 1110 cm^{-1} is due to C−N stretching vibration in tepa. The band of 1613 cm^{-1} in the hybrid nanoplates is attributed to the bending vibrations of N−H in tepa, which is larger than the value (1591 cm^{-1}) for raw tepa solvent, indicating the complexation of tepa with iron ions and the elongation of N−H bonds. It reveals the presence of organic tepa in the hybrid material. The relative molar ratio of Fe to Se in the hybrid nanoplates was examined by EDX elemental analysis (the inset of Figure 1a). The presence of Fe and Se as the only heavy elements is observed in the EDX spectrum, and the Fe/Se average atomic ratio is determined to be 43.23/56.77 (3.04:4) in good agreement with the stoichiometric ratio of Fe and Se in the starting materials. TGA curve in Figure 3a shows a small weight loss (~2.8 wt%) from room temperature to ~570 K due to a small amount of free tepa and other organic solvents absorbed on the surface of the hybrid nanoplates, and a sharp weight loss (13.1 wt%) between the onset temperature (T_{onset}) of ~570 K and the end temperature (T_{end}) of 726 K for decomposition,

due to the loss of the bonded tepa and a small amount of Se. Figure 3b represents that the product heated at 673 K consists of tetragonal β-Fe_3Se_4 nanoplates and monoclinic Fe_3Se_4, while that heated at 723 K consists of tetragonal β-Fe_3Se_4 nanoplates, monoclinic Fe_3Se_4 and hexagonal Fe_7Se_8. Monoclinic Fe_3Se_4 may be generated by a structural transition from the tetragonal β-Fe_3Se_4. Hexagonal Fe_7Se_8 was produced by a little loss of Se from these Fe_3Se_4 nanoplates. A phase transformation from monoclinic Fe_3Se_4 (T_C = 334 K) to hexagonal Fe_7Se_8 (T_C = 460 K) was observed in the thermal decomposition product of $(\beta\text{-}Fe_3Se_4)_4[Fe(teta)_{1.5}]$ due to loss of a slight Se [20]. According to Figure 3b, the thermal decomposition of hybrid precursor should be complete below 673 K and weight loss around 673 K was resulted from evaporation of tepa. The molar ratio of Fe_3Se_4 to tepa in the hybrid precursor was suggested to be calculated by removing the influence of the small amount of Se on the weight loss. We suppose that below 685 K, only a little higher than 673 K, there was no Se loss from both the tetragonal Fe_3Se_4 and the monoclinic Fe_3Se_4 nanoplates. As a result, the TG analysis would give a molar ratio of 3:1 for Fe_3Se_4 to tepa in the hybrid precursor. It suggests a chemical formula of $(Fe_3Se_4)_3$tepa for the present hybrid precursor.

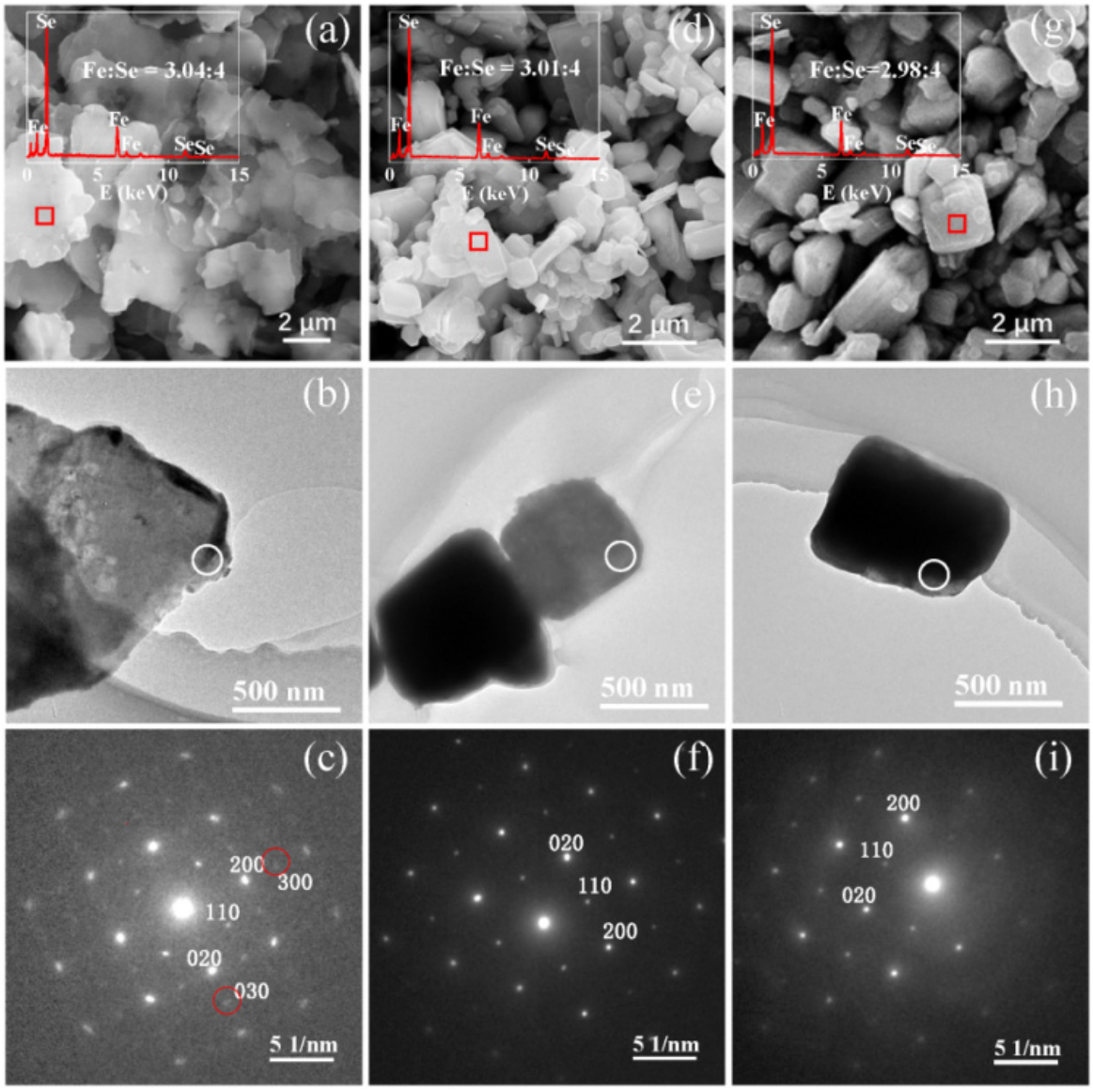

Figure 1. SEM image, TEM image and SAED pattern of (**a**–**c**) the $(\beta\text{-}Fe_2Se_3)_4[Fe(tepa)]$ hybrid precursor, (**d**–**f**) the as-synthetic β-Fe_3Se_4 nanoplates, and (**g**–**i**) the β-Fe_3Se_4 nanoplates annealed at 623 K.

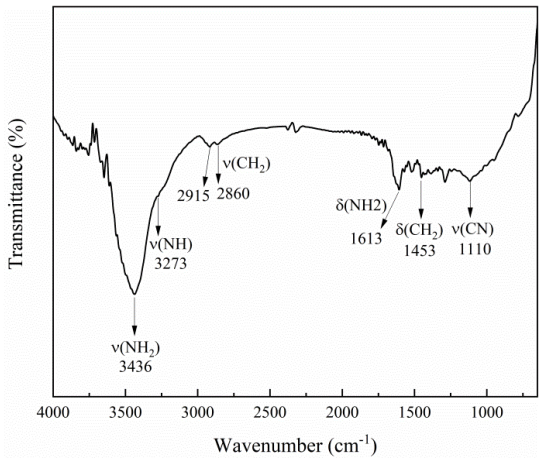

Figure 2. FTIR spectrum of the hybrid precursor.

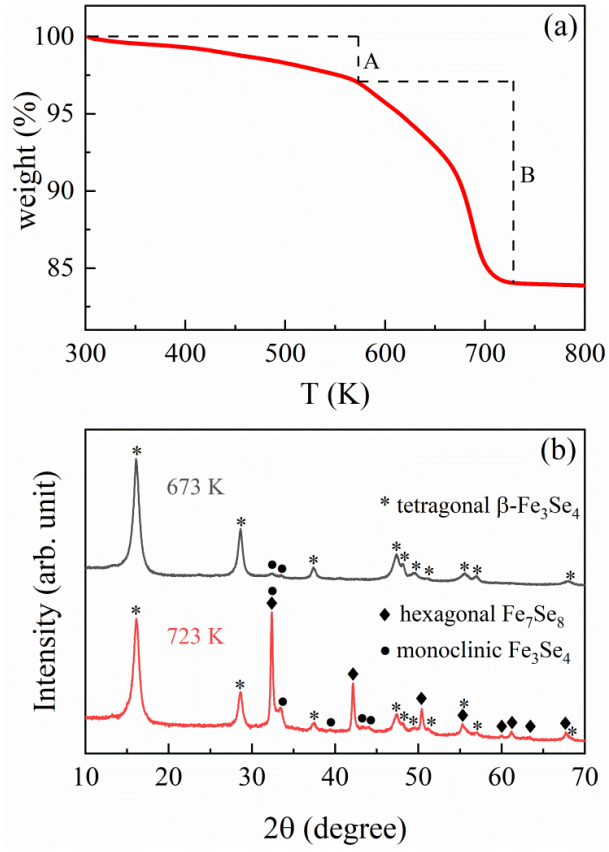

Figure 3. (**a**) TG curve of the hybrid precursor and (**b**) XRD patterns of the products decomposed at 673 and 723 K, respectively.

A SAED image of a hybrid nanoplate in Figure 1c reveals periodic crystal structure along the thickness direction. Compared to the previous $(\beta\text{-}Fe_3Se_4)_4[Fe(teta)_{1.5}]$ [20], a little obscure diffraction points marked by red circles in the SAED image may be caused by more iron vacancies in the hybrid nanoplate. Powder XRD pattern of the hybrid material (Figure 4a) reveals that all Bragg diffraction peaks can be refined and indexed by using the tetragonal structure with the space group I4cm (No. 108). The corresponding refinement process gave good R factors (R_p = 6.046%, R_{wp} = 9.609% and χ^2 = 1.732) and the crystal structure of the $(Fe_3Se_4)_3$tepa hybrid nanoplates is the same as that for previous $(\beta\text{-}Fe_3Se_4)_4[Fe(teta)_{1.5}]$ [20], in which two independent subsystems have been identified: $\beta\text{-}Fe_3Se_4$ superstructure and $Fe(teta)_{1.5}$ complex. Refined room-temperature lattice parame-

ters of the hybrid material are a = 8.642(0) Å and c = 19.40(3) Å, about 0.6% and 6.8% shrinkage along the a and c axes, respectively, compared with that of $(\beta\text{-}Fe_3Se_4)_4[Fe(teta)_{1.5}]$ [20]. The Fe/Se molar ratio in this hybrid material is 3:4, which deviates much from 3.25:4 for the $(\beta\text{-}Fe_3Se_4)_4[Fe(teta)_{1.5}]$, demonstrating that the inorganic building units in the present hybrid material differ from the $\beta\text{-}Fe_3Se_4$ superstructures. Based on the electron diffraction analysis on the tetragonal $\beta\text{-}Fe_{1-x}Se$ ($0.1 \leq x \leq 0.5$) superstructures in the reference [16] and our previous works [20,21], the tetragonal $\beta\text{-}Fe_2Se_3$ (x = 0.333) superstructure is the only possible fragment built in the present hybrid material. The SAED for $\beta\text{-}Fe_2Se_3$ superstructure is different from that of $\beta\text{-}Fe_3Se_4$ superstructures due to more ordered iron vacancies in $\beta\text{-}Fe_2Se_3$ than in $\beta\text{-}Fe_3Se_4$. However, when a SAED was taken along the c axis or the thickness direction of the present layered hybrid nanoplate, Fe atoms in $[Fe(tepa)]^{2+}$ complexes that overlap on iron vacancies of tetragonal $\beta\text{-}Fe_2Se_3$ superstructures could influence the observation of iron vacancy order of tetragonal $\beta\text{-}Fe_2Se_3$. As a result, Figure 1c represents a SAED image similar to that of $\beta\text{-}Fe_3Se_4$ superstructure. With the consideration of the unit cell size, atom composition, inorganic/organic unit molar ratio and electrical neutrality principles, we suggest that the most possible coordination for this new hybrid material is $(\beta\text{-}Fe_2Se_3)_4[Fe(tepa)]$, which is incorporated with inorganic $\left(\beta - Fe^{+2}_{0.5}Fe^{+3}_{1.5}Se^{-2}_{3}\right)^{2-}_{4}$ building units and organic $[Fe(tepa)]^{2+}$ complexes. Specifically, $[(\beta\text{-}Fe_2Se_3)_4]^{2-}$ layers are along the *ab* plane, while penda-dentate ligand tepa can saturate five vertices of the octahedral Fe coordination environment and leave one neighboring vertex unfilled. The unfilled vertex of Fe makes $[Fe(tepa)]^{2+}$ complexes coordinate with $[(\beta\text{-}Fe_2Se_3)_4]^{2-}$ layers by taking a horizontal configuration similar to previous $(\beta\text{-}Fe_3Se_4)_4[Fe(teta)_{1.5}]$ [20]. The $[Fe(tepa)]^{2+}$ complexes situate on top of the ordered Fe vacancies in the $[(\beta\text{-}Fe_2Se_3)_4]^{2-}$ layers, which causes shifts of the atoms in $[Fe(tepa)]^{2+}$ complexes to these iron vacancies and thus smaller unit cell parameters [21].

SEM image (Figure 1d) illustrates that the $\beta\text{-}Fe_3Se_4$ nanoplates synthesized by thermal decomposition of hybrid nanoplates at 603 K are in a square shape with a varied particle size from several hundred nanometers to 3 μm. The thicknesses of some $\beta\text{-}Fe_3Se_4$ nanoplates are obviously bigger than those of hybrid precursor, possibly due to thermal decomposition of several adjacent hybrid nanoplates to a $\beta\text{-}Fe_3Se_4$ nanoplate. From the EDX spectrum (the inset of Figure 1d), the Fe/Se atomic ratio is determined in average to be 42.99/57.01 (3.01:4) for the synthetic $\beta\text{-}Fe_3Se_4$ nanoplates, which is in good agreement with the stoichiometric ratio of Fe and Se in the hybrid precursor. The oxidation states of Fe and Se species have been evaluated by X-ray photoelectron spectroscopy (XPS) (Figure 5). The binding energies of C 1s at about 285 and 285.5 eV in Figure 5a revealed the amorphous carbon and the C-N in tepa [22] absorbed on the surface of the as-synthetic $\beta\text{-}Fe_3Se_4$ nanoplates. Based on the calibration of amorphous carbon at 285 eV, the Fe 2p and the Se 3d spectra were shown in Figure 5b,c, respectively. The Fe 2p spectrum (Figure 5b) contains two asymmetric peaks due to the spin-orbit splitting, which can be assigned to Fe $2p_{3/2}$ at 711.0 eV and Fe $2p_{1/2}$ at 724.7 eV. Both Fe $2p_{3/2}$ and Fe $2p_{1/2}$ peaks can be further deconvoluted into two sub-peaks Fe^{2+} ($2p_{3/2}$ at 710.0 eV, $2p_{1/2}$ at 723.6 eV) and Fe^{3+} ($2p_{3/2}$ at 711.8 eV, $2p_{1/2}$ at 725.4 eV) [23]. Satellite peaks can be detected at 715.9 and 719.5 eV for Fe^{2+} $2p_{3/2}$ and Fe^{3+} $2p_{3/2}$, respectively. According to the fitting area for the Fe^{2+} and Fe^{3+} ions, the molar ratio of Fe^{2+}/Fe^{3+} in the as-synthetic $\beta\text{-}Fe_3Se_4$ nanoplates was estimated to be 1:1.9, which is close to the Fe^{2+}/Fe^{3+} of 1:2 for $\beta\text{-}Fe_3Se_4$ based on the electrical neutrality principles. Figure 5c shows the Se 3d peak at 55.1 eV, indicating the presence of Se-Fe-Se [24,25], which could be deconvoluted into Se $3d_{5/2}$ at 54.7 eV and Se $3d_{3/2}$ at 55.6 eV. For the $\beta\text{-}Fe_3Se_4$ nanoplates annealed at 623 K, the C 1s (at 285 and 285.5 eV), Fe 2p with Fe^{2+} ($2p_{3/2}$ at 710.2 eV, $2p_{1/2}$ at 723.8 eV) and Fe^{3+} ($2p_{3/2}$ at 711.8 eV and $2p_{1/2}$ at 725.4 eV) and Se 3d ($3d_{5/2}$ at 55.1 eV and $3d_{3/2}$ at 56.0 eV) spectra were also analyzed and presented in Figure 5d–f, which are similar to the results of the as-synthetic $\beta\text{-}Fe_3Se_4$ nanoplates. Moreover, the satellite peaks can be detected at 715.2 and 719.7 eV for Fe^{2+} $2p_{3/2}$ and Fe^{3+} $2p_{3/2}$ in the annealed sample, respectively. TEM image (Figure 1e) and the corresponding SAED pattern (Figure 1f) reveal periodic crystal structure of a $\beta\text{-}Fe_3Se_4$ nanoplate in the thickness direction

along the c axis. Compared to the SAED pattern of the hybrid precursor (Figure 1c), the diffraction points for the β-Fe_3Se_4 nanoplate become clear and distinguishable (Figure 1f). However, the SAED pattern is similar to the superconducting β-FeSe nanosheets reported previously [13], but much different from that of β-Fe_3Se_4 superstructure with ordered iron vacancies in the $(β\text{-}Fe_3Se_4)_4[Fe(teta)_{1.5}]$ [20]. The formation of β-Fe_3Se_4 nanoplates may follow a thermal decomposition reaction of $(Fe_2Se_3)_4[Fe(tepa)] = 4Fe_2Se_3 + Fe + tepa$ and a diffusion reaction of $4Fe_2Se_3 + Fe = 3Fe_3Se_4$. During the reactions, Fe atoms produced by thermal decomposition of $[Fe(tepa)]^{2+}$ complexes may randomly diffuse and fill in the iron vacancies of β-Fe_2Se_3, which would create a random distribution of iron vacancies in the as-synthetic β-Fe_3Se_4 nanoplates. As a result, the absented (h00) and (0k0) with h odd and k odd originating from iron vacancy order are not visible again in the SAED of our as-synthetic β-Fe_3Se_4 nanoplates recorded along the c direction, which is much different from that of previous β-Fe_3Se_4 superstructure with iron vacancy order [20]. The XRD of the as-synthetic β-Fe_3Se_4 nanoplates was refined in Figure 4b based on the model for the β-FeSe [2,13]. The corresponding refinement process gave good R factors (R_p = 3.557%, R_{wp} = 5.099% and χ^2 = 0.657) and refined lattice parameters at room temperature are a = 3.775(8) Å and c = 5.514(5) Å for the as-synthetic β-Fe_3Se_4 nanoplates, about 0.28% expansion along the a and b axes due to Fe vacancies but almost the same along the c axis comparing with that of superconducting β-FeSe [13]. The disordered distributions of iron vacancies are currently under investigation.

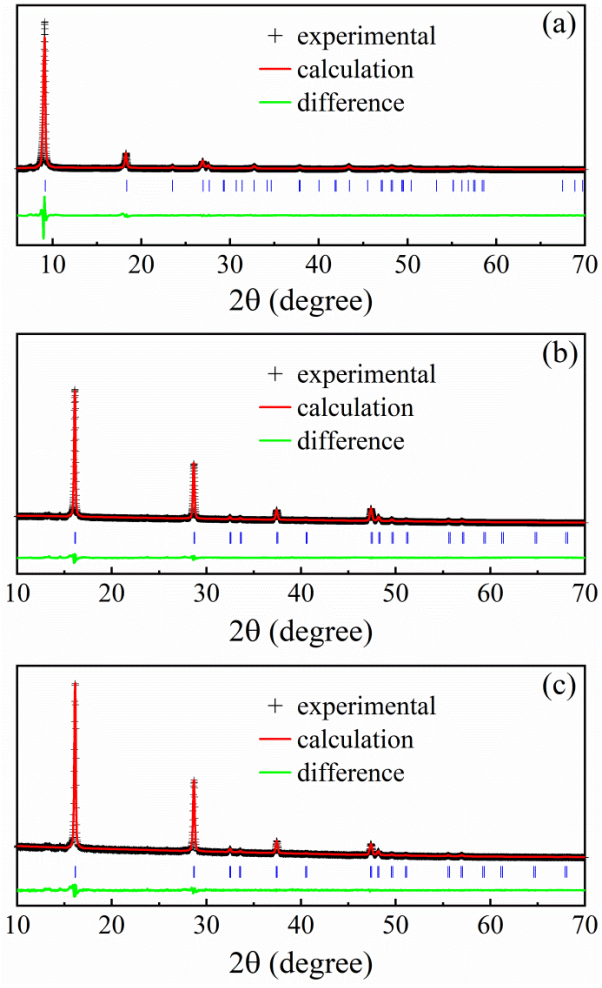

Figure 4. Powder XRD pattern of (**a**) the hybrid precursor, (**b**) the as-synthetic β-Fe_3Se_4 nanoplates, and (**c**) the β-Fe_3Se_4 nanoplates annealed at 623 K, recorded at room temperature (solid crosses) with Rietveld refinements and difference curves.

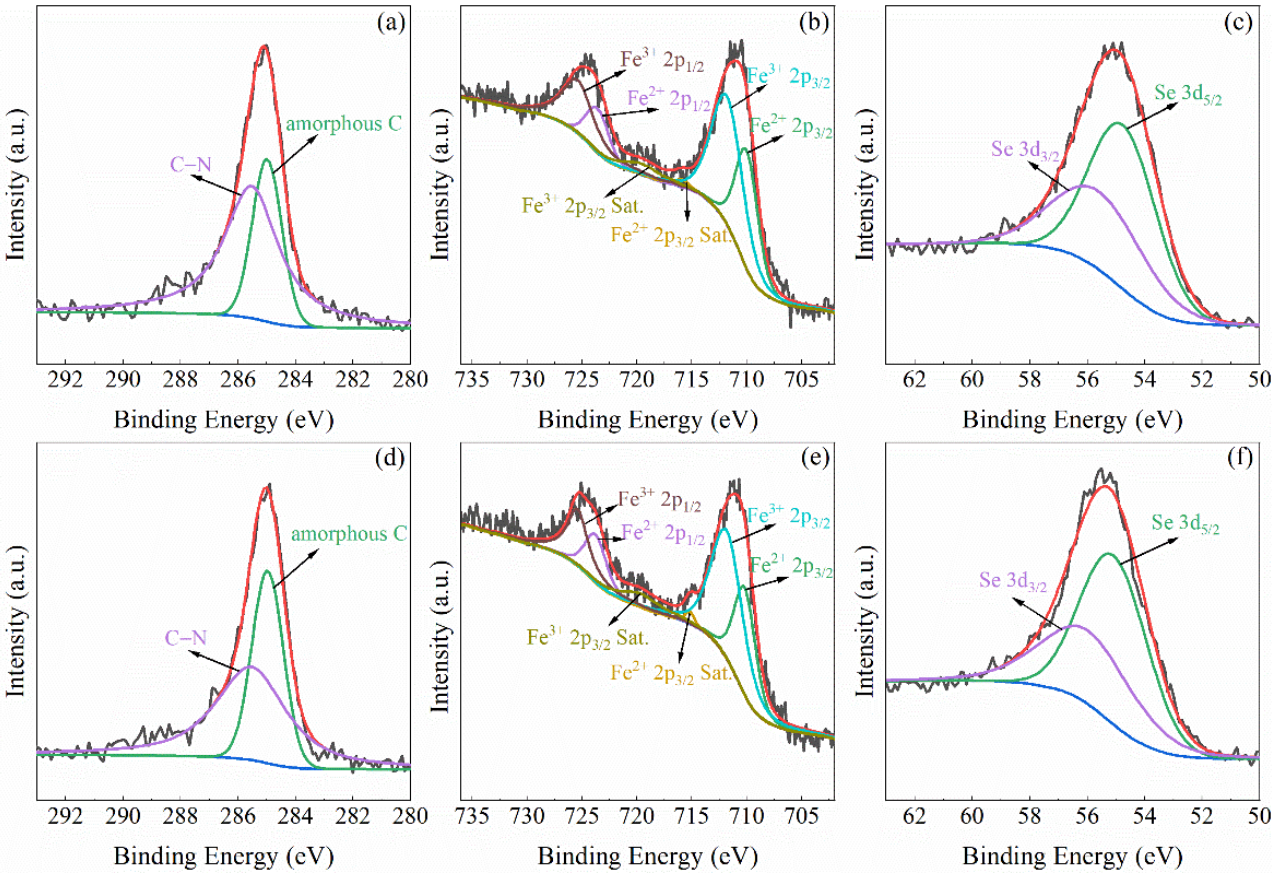

Figure 5. XPS spectrum of (**a**) C 1s, (**b**) Fe 2p and (**c**) Se 3d for the as-synthetic β-Fe_3Se_4 nanoplates and (**d**) C 1s, (**e**) Fe 2p and (**f**) Se 3d for the annealed β-Fe_3Se_4 nanoplates.

3.2. Magnetic Properties

Figure 6a presents isothermal field (H) dependence of magnetization (M) of the hybrid precursor, showing a weak ferromagnetic feature at a low magnetic field range. The small hysteresis loops of the hybrid material reveal the ferromagnetic characteristics in the temperature range between 10 K and 370 K. The coercivity (H_C) and remanence magnetization are 297 Oe and 0.006 emu g^{-1} at 370 K, respectively, which increase to 309 Oe and 0.017 emu g^{-1} at 10 K. The magnetizations at a high magnetic field range increase linearly with increasing the magnetic field even up to the maximum magnetic field of 50 kOe. This linear field dependence of the magnetization at high field range is not contrary to the ferrimagnetic compounds, in which strong antiferromagnetic coupling between different magnetic sublattices prevents their full alignment by the magnetic field [20]. Figure 6b presents the temperature (T) dependence of magnetization of the hybrid material recorded from 10 and 370 K in the ZFC/FC processes under a magnetic field of 0.1 and 50 kOe, respectively. The ZFC/FC curves at a magnetic field of 0.1 kOe exhibit a divergence below ~250 K, while the divergence temperature decreases to ~60 K as the ZFC/FC curves were measured in a high magnetic field of 50 kOe. The FC curve shows a smooth decrease in magnetization with raising the temperature from 10 to 370 K. It suggests no magnetic transition of this hybrid precursor below 370 K, and its T_C should be higher than 370 K. Such a room-temperature ferrimagnetic behavior is similar to those of our previous ordered inorganic–organic hybrid materials $(\beta\text{-}Fe_3Se_4)_4[Fe(teta)_{1.5}]$ and the $Fe_3Se_4(dien)_2$ [20,21].

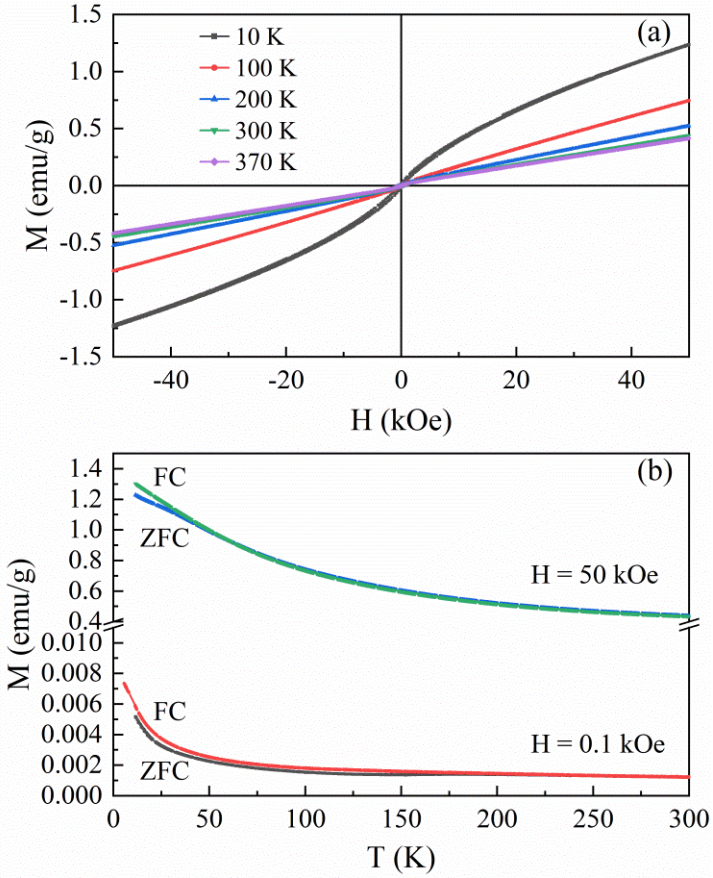

Figure 6. (**a**) Hysteresis loops and (**b**) temperature dependence of magnetization for the hybrid precursor.

Figure 7 reveals the magnetic properties of the as-synthetic β-Fe_3Se_4 nanoplates, which are obviously different from their hybrid precursor. Figure 7a shows that both ZFC and FC magnetizations recorded at a magnetic field of 50 kOe in a temperature range from 10 to 370 K decrease with increasing the temperature to about 140 and then increase to 370 K. Such a behavior is also observed in the FC magnetization curve in a magnetic field of 140 kOe with an inflection point temperature shifting to about 125 K. High-temperature magnetization measurements in Figure 7b show reversible temperature dependence of magnetization below 420 K, which becomes irreversible above 420 K. It indicates that the as-synthetic β-Fe_3Se_4 nanoplates are metastable at room temperature and their magnetism changes at a temperature higher than 420 K. Isothermal field dependence of magnetization between −50 and 50 kOe in Figure 7c shows a weak S-shape in the MH curve recorded at 140 K and a small hysteresis loop at 10 K, suggesting a weak ferromagnetic feature of the as-synthetic β-Fe_3Se_4 nanoplates below 140 K. Above this temperature, a linear field dependence of magnetization was observed in the MH curves recorded at a temperature between 300 and 320 K (Figure 7c). The linear field dependence of magnetization was also observed at 370 K and higher magnetic field ranges from −140 to 140 kOe (Figure 7d). Considering the increase in magnetization with increasing the temperature from 140 to 420 K (Figure 7a,b), the linear field dependence of magnetization suggests an antiferromagnetism of the as-synthetic β-Fe_3Se_4 nanoplates. Hysteresis loop recorded after field-cooled from 370 to 10 K at 140 kOe shows an exchange bias effect with a coercivity of 7.83 kOe and an exchange bias field of 2.55 kOe (Figure 7d), further revealing the presence of ferromagnetic and antiferromagnetic components in the as-synthetic β-Fe_3Se_4 nanoplates. The disordered distribution of iron vacancies in the as-synthetic β-Fe_3Se_4 nanoplates may be the reason that creates the different magnetic spin configurations. Besides a magnetic irreversibility (Figure 7b), temperature dependence of magnetization in the process cooling from 470 to 300 K shows no magnetic transition for the

β-Fe_3Se_4 sample. However, after the sample was heated to 600 K, a magnetic transition was observed at about 335 K in the cooling process from 600 to 300 K. Such a magnetic transition temperature is in good agreement with the T_C for monoclinic Fe_3Se_4 [8], suggesting that a crystal structure transition from tetragonal β-Fe_3Se_4 to monoclinic Fe_3Se_4 occurred in the high-temperature magnetic measurement.

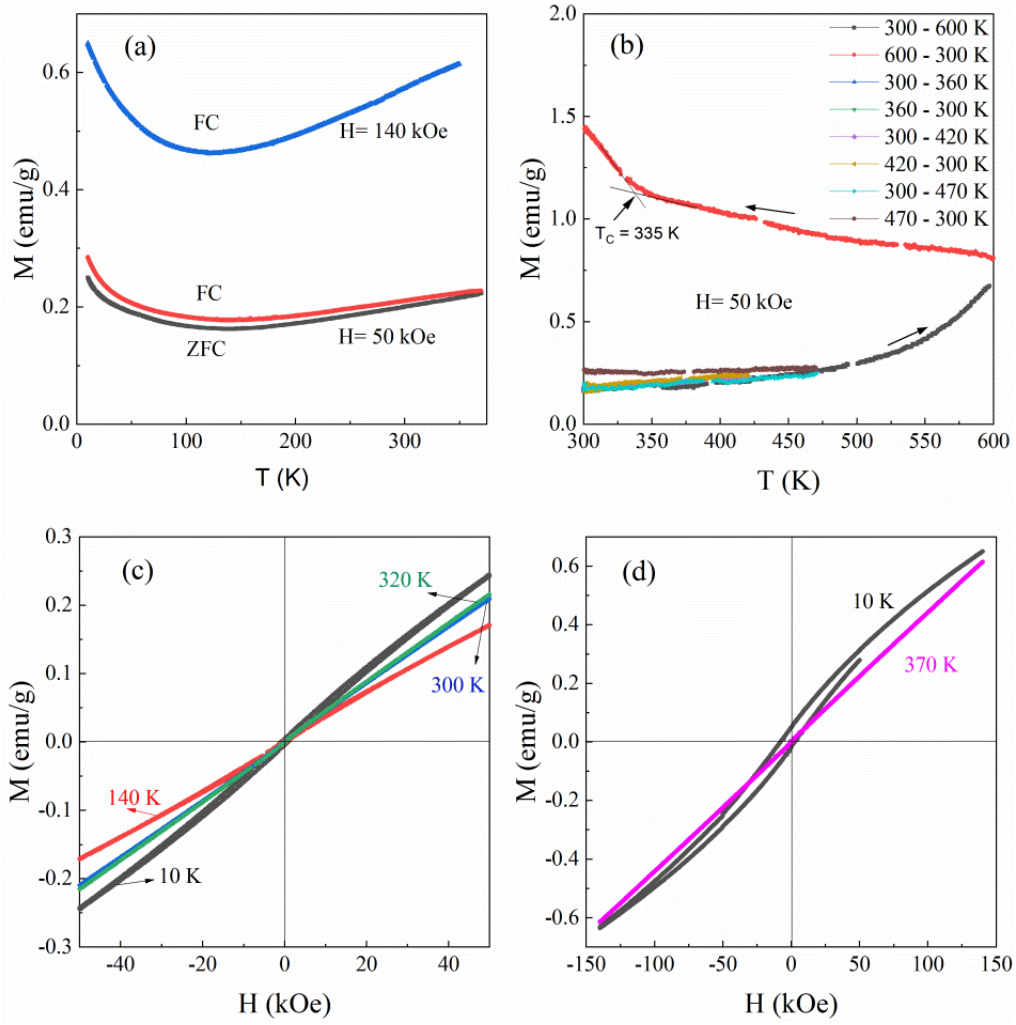

Figure 7. Magnetic properties of the as-synthetic β-Fe_3Se_4 nanoplates. (**a**) Temperature dependence of ZFC and FC magnetization in a temperature range between 10 and 370 K. (**b**) Temperature dependence of magnetization in both heating and cooling within different temperature ranges. (**c**) Hysteresis loops recorded in a magnetic field between −50 and 50 kOe at different temperatures. (**d**) Hysteresis loops recorded in a magnetic field between −140 and 140 kOe at 370 K and after a FC process at a magnetic field of 140 kOe from 370 to 10 K.

Figure 7b shows a thermal instability of the as-synthetic β-Fe_3Se_4 nanoplates at a temperature higher than 420 K. To examine the magnetic irreversibility in the heating process from 300 to 470 K and in the cooling process from 470 to 300 K, we annealed the as-synthetic β-Fe_3Se_4 nanoplates in a sealed SiO_2 tube in an argon atmosphere at 623 K (just a little higher than the synthetic temperature of 603 K) for 1 h. Figure 4c represents the XRD pattern of the annealed β-Fe_3Se_4 nanoplates. The corresponding refinement process gave good R factors (R_p = 5.098%, R_{wp} = 6.851% and χ^2 = 1.774) for the annealed sample. In the case of the annealed β-Fe_3Se_4 nanoplates, refined lattice parameters at room temperature are a = 3.779(3) Å and c = 5.513(8) Å, almost the same as those of the as-synthetic material. Both the XRD pattern (Figure 4c) and the structure characteristics (Figure 1g–i) for the

annealed sample are similar to those of the as-synthetic β-Fe_3Se_4 nanoplates, indicating few changes in the unit cell parameters. Figure 8a plots the temperature dependence of magnetization of the annealed β-Fe_3Se_4 nanoplates recorded in the ZFC/FC curves between 10 and 370 K under a magnetic field of 0.1 and 50 kOe, respectively. The ZFC/FC curves under 0.1 kOe exhibit a divergence below ~250 K, while the divergence temperature decreases to ~60 K in 50 kOe. The FC curves show a smooth decrease in magnetization with raising the temperature from 10 to 370 K, suggesting a ferromagnetic feature of the annealed β-Fe_3Se_4 nanoplates below 370 K. Therefore, the T_C of the annealed β-Fe_3Se_4 nanoplates should be higher than 370 K. The magnetization in Figure 8b shows a slight decrease with increasing temperature to about 470 K and then an increase with increasing temperature to 600 K, almost the same as the temperature dependence of magnetization for the β-Fe_3Se_4 nanoplates experienced a heating process from 300 to 470 K as shown in Figure 7b. When the annealed sample was cooled down from 600 K, a magnetic transition at about 335 K corresponding to monoclinic β-Fe_3Se_4 phase was also observed. It suggests that heat treatment at 623 K results in a magnetic change from the antiferromagnetism for the as-synthetic β-Fe_3Se_4 nanoplates to the ferrimagnetism for the annealed β-Fe_3Se_4 nanoplates. Hysteresis loops of the annealed β-Fe_3Se_4 nanoplates in Figure 8c present the ferrimagnetism at a temperature range from 10 to 300 K. The saturation magnetization (M_S) and coercivity (H_C) for the annealed β-Fe_3Se_4 nanoplates increase from 0.7 emu/g and 0.13 kOe at 300 K to 0.8 emu/g and 2.45 kOe at 10 K. Compared to monoclinic Fe_3Se_4, the reduced saturation magnetization for the annealed β-Fe_3Se_4 nanoplates may be ascribed to different spin configurations of Fe atoms in this tetragonal phase. Moreover, the coercivity values of the annealed β-Fe_3Se_4 nanoplates are much smaller than the previous results for the monoclinic Fe_3Se_4 nanoplatelets with the H_C of 40 and 4 kOe, respectively, at 10 and 300 K [4]. The different coercivity values may originate from the difference in grain sizes and stoichiometry. However, the unusually large coercivity for monoclinic Fe_3Se_4 nanostructure significantly depends on its uniaxial magnetocrystalline anisotropy [7]. Figure 8 further reveals an effect of a heat-treatment at a temperature of 623 K, only a little higher than the synthetic temperature (603 K), on the magnetic properties of the annealed β-Fe_3Se_4 nanoplates, which is much different from those of the as-synthetic β-Fe_3Se_4 nanoplates. The change of the magnetic properties should be resulted from the varied spin configurations for these samples under a thermal excitation.

Moreover, Figure 8b shows a high magnetization of about 1 emu/g at a magnetic field of 50 kOe at 600 K, which is larger than the M_S measured at 300 K. Such a high magnetization should be related to the annealed tetragonal β-Fe_3Se_4 temperature, but not monoclinic Fe_3Se_4 due to 600 K being much higher than the T_C of the monoclinic phase. The XRD pattern of the product decomposed at 673 K indicates that the product consists of a main phase of tetragonal β-Fe_3Se_4 and a minor phase of monoclinic Fe_3Se_4 (Figure 3b). It suggests that the T_C of the annealed tetragonal β-Fe_3Se_4 is higher than 600 K. However, tetragonal β-Fe_3Se_4 is metastable at a temperature higher than 470 K, which will transform to monoclinic Fe_3Se_4 through a change of crystal symmetry and hexagonal Fe_7Se_8 through loss of Se atoms. The phase evolution seriously relates to the annealing temperature and the annealing period. Although the Curie temperature is an important factor to a magnet, the T_C of the annealed tetragonal β-Fe_3Se_4 is not determined at present due to the absence of single phase tetragonal β-Fe_3Se_4 nanoplates at higher temperatures.

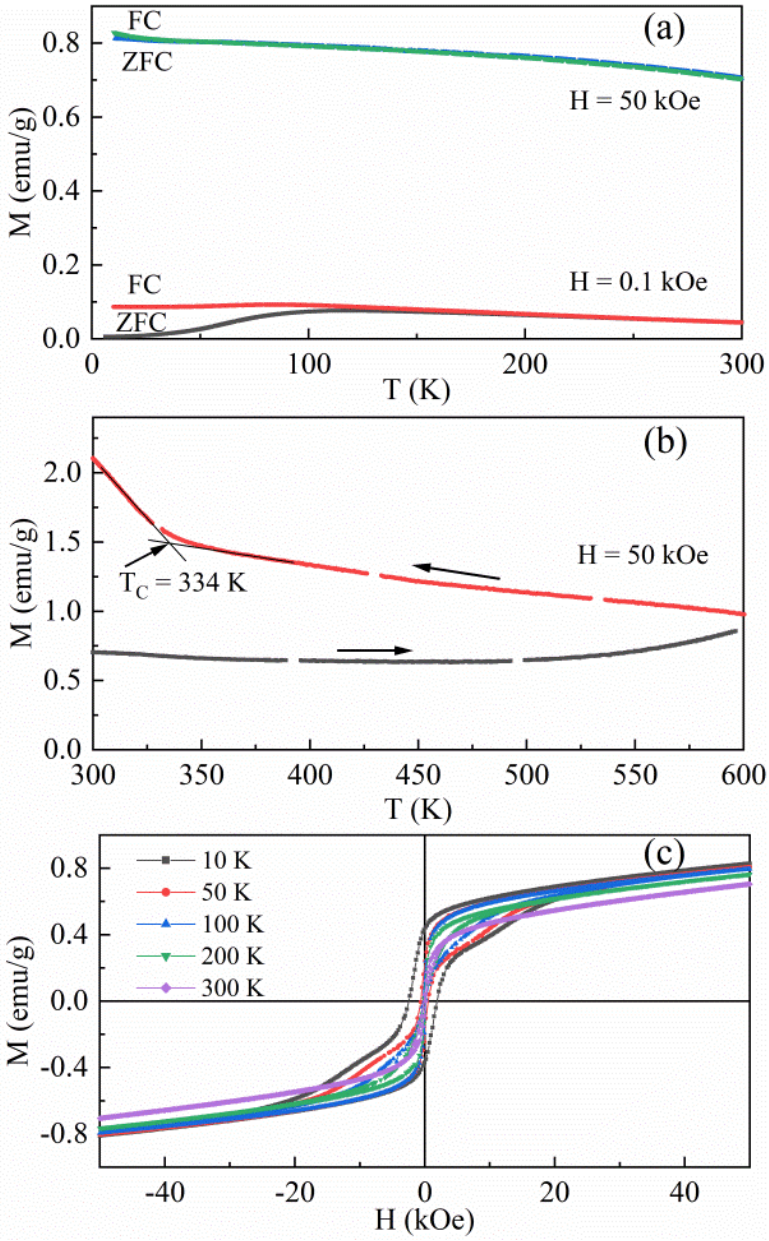

Figure 8. Magnetic properties of the annealed β-Fe_3Se_4 nanoplates. (**a**) Temperature dependence of ZFC and FC magnetization in a temperature range between 10 and 370 K. (**b**) Temperature dependence of magnetization in both heating and cooling in a temperature range from 300 to 600 K. (**c**) Hysteresis loops recorded in a magnetic field between −50 and 50 kOe at different temperatures.

The similarity and differences between tetragonal β-Fe_3Se_4 and the more extensively investigated monoclinic Fe_3Se_4. Despite the same chemical stoichiometry, the as-synthetic tetragonal β-Fe_3Se_4 is antiferromagnetic at room temperature, while the annealed tetragonal β-Fe_3Se_4 and the monoclinic Fe_3Se_4 are ferrimagnetic materials. The present tetragonal β-Fe_3Se_4 nanoplates are much different from the components in the intercalated compounds $AFe_{1.5}Se_2$ [17] and the inorganic building units in ordered inorganic–organic (β-Fe_3Se_4)$_4$[$Fe(teta)_{1.5}$] hybrid material [20]. Besides the strong 2D shape anisotropy of the nanoplates, the ferrimagnetic materials may have different magnetocrystalline anisotropies mainly due to different crystal symmetries. Previously, substitution of Se with Te in tetragonal FeSe results in an obvious enhancement of superconducting critical transition temperature [26]. Conversely, the Fe ions in monoclinic Fe_3Se_4 can be easily substituted by other transition metals to form different monoclinic phases with varying magnetic

properties [27]. For example, $Fe_{3-x}Cr_xSe_4$ ($0 \leq x \leq 2$) are hard magnets with a maximum magnetocrystalline anisotropy of 1.2×10^6 erg/cm^3 at x = 0.5 [9,10]. This substitution of Fe with other transition-metal ions should be also possible within tetragonal β-Fe_3Se_4. Our investigations reveal the dependence of magnetism of tetragonal structure of β-Fe_3Se_4 and monoclinic structure of Fe_3Se_4 on their crystal structures, which may originate from the difference distributions of iron vacancies. Other interesting physical properties originating from the varied crystal symmetries and distributions of iron vacancies are currently under investigation.

4. Conclusions

In conclusion, we have developed a facile protocol for synthesizing tetragonal β-Fe_3Se_4 nanoplates by thermal decomposition of a new ordered inorganic–organic (β-Fe_2Se_3)$_4$[Fe(tepa)] hybrid material in the high-temperature organic-solution-phase process. The ordered inorganic–organic (β-Fe_2Se_3)$_4$[Fe(tepa)] hybrid material is in a tetragonal crystal structure with a space group I4cm (108), while the as-synthetic tetragonal β-Fe_3Se_4 nanoplates have the layered crystal structure with the P4/nmm space group. The as-synthetic β-Fe_3Se_4 nanoplates show the antiferromagnetism in a temperature between 120 and 420 K but a ferrimagnetism below ~120 K. The as-synthetic β-Fe_3Se_4 nanoplates are metastable, which experienced an irreversible magnetic transition at about 470 K. The annealed β-Fe_3Se_4 nanoplates are in the ferrimagnetism between 10 and 470 K. Varied magnetic properties of tetragonal β-Fe_3Se_4 nanoplates are ascribed to disordered distribution of iron vacancies. Moreover, different magnetic properties of tetragonal structure of Fe_3Se_4 and monoclinic structure of Fe_3Se_4 should be mainly created by the different crystal symmetries.

Author Contributions: Conceptualization, D.L. and Z.Z.; methodology, D.L. and Q.K.; software, Q.K.; validation, X.M. and X.S.; investigation, Q.K., B.Z., B.Y., Y.Z. and Z.L.; resources, D.L.; data curation, Q.K.; writing—original draft preparation, D.L. and Q.K.; writing—review and editing, D.L. and Z.Z.; supervision, D.L. and Z.Z.; project administration, D.L.; funding acquisition, D.L. and Z.Z. All authors have read and agreed to the published version of the manuscript.

Funding: The research was supported by the National Natural Science Foundation of China under grants no. 51971221, 52031014, and the National Key R&D Program of China (no. 2017YFA0206302, 2017YFA0700702), Ministry of Science and Technology of China.

Data Availability Statement: Data are contained within the article.

Conflicts of Interest: The authors declare no conflict of interest.

References

1. Dietl, T. Ferromagnetic semiconductors. *Semicond. Sci. Tech.* **2002**, *17*, 377–392. [CrossRef]
2. Hsu, F.C.; Luo, J.Y.; Yeh, K.W.; Chen, T.K.; Huang, T.W.; Wu, P.M.; Lee, Y.C.; Huang, Y.L.; Chu, Y.Y.; Yan, D.C.; et al. Superconductivity in the PbO-type structure α-FeSe. *Proc. Natl. Acad. Sci. USA* **2008**, *105*, 14262–14264. [CrossRef] [PubMed]
3. Liu, K.W.; Zhang, J.Y.; Shen, D.Z.; Shan, C.X.; Li, B.H.; Lu, Y.M.; Fan, X.W. Electronic and magnetic properties of FeSe thin film prepared on GaAs (001) substrate by metal-organic chemical vapor deposition. *Appl. Phys. Lett.* **2007**, *90*, 262503. [CrossRef]
4. Zhang, H.W.; Long, G.; Li, D.; Sabirianov, R.; Zeng, H. Fe_3Se_4 Nanostructures with giant coercivity synthesized by solution chemistry. *Chem. Mater.* **2011**, *23*, 3769–3774. [CrossRef]
5. Abd-El Aal, M.M. Magnetic-properties of $(Fe_{1-x}M_x)_7Se_8$. *J. Mater. Sci* **1988**, *23*, 3490–3494. [CrossRef]
6. Li, D.; Jiang, J.J.; Liu, W.; Zhang, Z.D. Positive magnetoresistance in Fe_3Se_4 nanowires. *J. Appl. Phys.* **2011**, *109*, 07C705. [CrossRef]
7. Long, G.; Zhang, H.W.; Li, D.; Sabirianov, R.; Zhang, Z.D.; Zeng, H. Magnetic anisotropy and coercivity of Fe_3Se_4 nanostructures. *Appl. Phys. Lett.* **2011**, *99*, 202103. [CrossRef]
8. Li, D.; Li, S.J.; Zhou, Y.T.; Bai, Y.; Zhu, Y.L.; Ren, W.J.; Long, G.; Zeng, H.; Zhang, Z.D. Magnetization reversal and coercivity of Fe_3Se_4 nanowire arrays. *J. Appl. Phys.* **2015**, *117*, 17E702. [CrossRef]
9. Li, S.J.; Li, D.; Liu, W.; Zhang, Z.D. High Curie temperature and coercivity performance of $Fe_{3-x}Cr_xSe_4$ nanostructures. *Nanoscale* **2015**, *7*, 5395–5402. [CrossRef]
10. Li, D.; Li, S.J.; Dong, B.J.; Yang, T.; Liu, W.; Zhang, Z.D. Large magnetocrystalline anisotropy of $Fe_{3-x}Cr_xSe_4$ single crystals due to Cr substitution. *Epl-Europhys. Lett.* **2015**, *109*, 37004. [CrossRef]
11. Andresen, A.F.; Laar, B.V. Magnetic Structure of Fe_3Se_4. *Acta Chem. Scand.* **1970**, *24*, 2435–2439. [CrossRef]

12. Mizuguchi, Y.; Tomioka, F.; Tsuda, S.; Yamaguchi, T.; Takano, Y. Superconductivity at 27 K in tetragonal FeSe under high pressure. *Appl. Phys. Lett.* **2008**, *93*, 152505. [CrossRef]
13. Li, D.; Pan, D.S.; Liu, W.L.; Li, X.X.; Chen, M.L.; Li, S.J.; Li, Y.; Tan, J.; Sun, D.M.; Wang, Z.H.; et al. Controllable Phase Transition for Layered β-FeSe superconductor synthesized by solution chemistry. *Chem. Mater.* **2017**, *29*, 842–848. [CrossRef]
14. Wu, X.J.; Zhang, Z.Z.; Zhang, J.Y.; Li, B.H.; Ju, Z.G.; Lu, Y.M.; Li, B.S.; Shen, D.Z. Two-carrier transport and ferromagnetism in FeSe thin films. *J. Appl. Phys.* **2008**, *103*, 113501. [CrossRef]
15. Mendoza, D.; Benitez, J.L.; Morales, F.; Escudero, R. Magnetic anomaly in superconducting FeSe. *Solid State Commun.* **2010**, *150*, 1124–1127. [CrossRef]
16. Chen, T.K.; Chang, C.C.; Chang, H.H.; Fang, A.H.; Wang, C.H.; Chao, W.H.; Tseng, C.M.; Lee, Y.C.; Wu, Y.R.; Wen, M.H.; et al. Fe-vacancy order and superconductivity in tetragonal β-$Fe_{1-x}Se$. *Proc. Natl. Acad. Sci. USA* **2014**, *111*, 63–68. [CrossRef]
17. Yan, X.W.; Gao, M.A.; Lu, Z.Y.; Xiang, T. Electronic structures and magnetic order of ordered-Fe-vacancy ternary iron selenides $TlFe_{1.5}Se_2$ and $AFe_{1.5}Se_2$ (A. = K, Rb, or Cs). *Phys. Rev. Lett* **2011**, *106*, 087005. [CrossRef]
18. Pak, C.; Kamali, S.; Pham, J.; Lee, K.; Greenfield, J.T.; Kovnir, K. Chemical Excision of Tetrahedral $FeSe_2$ Chains from the Superconductor FeSe: Synthesis, Crystal Structure, and Magnetism of $Fe_3Se_4(en)_2$. *J. Am. Chem. Soc.* **2013**, *135*, 19111–19114. [CrossRef]
19. Greenfield, J.T.; Pak, C.; Kamali, S.; Lee, K.; Kovnir, K. Control over connectivity and magnetism of tetrahedral $FeSe_2$ chains through coordination Fe-amine complexes. *Chem. Commun.* **2015**, *51*, 5355–5358. [CrossRef]
20. Pan, D.S.; Li, Y.; Han, Z.; Li, B.; Wang, C.W.; Yang, T.; Li, D.; Choi, C.J.; Zhang, Z.D. Organic-inorganic hybrid (β-$Fe_3Se_4)_4$[$Fe(teta)_{1.5}$] (teta = triethylenetetramine) nanoplates: Solution synthesis and magnetic properties. *Chem. Mater.* **2018**, *30*, 8975–8982. [CrossRef]
21. Pan, D.S.; Kuang, Q.F.; Tong, P.; Tong, W.; Fan, L.B.; Zhao, J.; Li, D.; Choi, C.J.; Zhang, Z.D. Self-assembly of 1D $FeSe_2$ chains and $Fe(dien)_2$ complexes for ferrimagnetic inorganic-organic hybrid cuboids. *J. Magn. Magn. Mater.* **2022**, *542*, 168585. [CrossRef]
22. Ren, Q.; Shen, X.; Zhang, J.; Liu, J. Simultaneous Reduction and Covalent Combining of Tetraethylenepentamine on Graphene Oxide. *IOP Conf. Ser. Mater. Sci. Eng.* **2019**, *472*, 012096. [CrossRef]
23. Torres-Cavanillas, R.; Morant-Giner, M.; Escorcia-Ariza, G.; Dugay, J.; Canet-Ferrer, J.; Tatay, S.; Cardona-Serra, S.; Gimenez-Marques, M.; Galbiati, M.; Forment-Aliaga, A.; et al. Spin-crossover nanoparticles anchored on MoS_2 layers for heterostructures with tunable strain driven by thermal or light-induced spin switching. *Nat. Chem.* **2021**, *13*, 1101–1109. [CrossRef] [PubMed]
24. Liu, J.W.; Xiao, S.H.; Li, X.Y.; Li, Z.Z.; Li, X.R.; Zhang, W.S.; Xiang, Y.; Niu, X.B.; Chen, J.S. Interface engineering of Fe_3Se_4/FeSe heterostructure encapsulated in electrospun carbon nanofibers for fast and robust sodium storage. *Chem. Eng. J.* **2021**, *417*, 129279. [CrossRef]
25. Zheng, Q.L.; Cheng, X.; Li, H.Y. Microwave Synthesis of High Activity $FeSe_2$/C Catalyst toward Oxygen Reduction Reaction. *Catalysts* **2015**, *5*, 1079–1091. [CrossRef]
26. Fang, M.H.; Pham, H.M.; Qian, B.; Liu, T.J.; Vehstedt, E.K.; Liu, Y.; Spinu, L.; Mao, Z.Q. Superconductivity close to magnetic instability in $Fe(Se_{1-x}Te_x)_{0.82}$. *Phys. Rev. B* **2008**, *78*, 224503. [CrossRef]
27. Sen Bishwas, M.; Das, R.; Poddar, P. Large Increase in the Energy Product of Fe_3Se_4 by Fe-Site Doping. *J. Phys. Chem. C* **2014**, *118*, 4016–4022. [CrossRef]